arXiv:1008.3736v2 [physics.ins-det] 24 Aug 2010

arXiv: 1008.3736 [physics.ins-det] 26 April 2010

Gaseous Detectors: recent developments and applications[a]

Maxim Titov
CEA Saclay, DSM/IRFU/SPP, 91191 Gif sur Yvette, France



Since long time, the compelling scientific goals of future high energy physics experiments were a driving factor in the development of advanced detector technologies. A true innovation in detector instrumentation concepts came in 1968, with the development of a fully parallel readout for a large array of sensing elements - the Multiwire Proportional Chamber (MWPC), which earned Georges Charpak a Nobel prize in physics in 1992. Since that time radiation detection and imaging with fast gaseous detectors, capable of economically covering large detection volume with low mass budget, have been playing an important role in many fields of physics. Advances in photo-lithography and micro-processing techniques in the chip industry during the past decade triggered a major transition in the field of gas detectors from wire structures to Micro-Pattern Gas Detector (MPGD) concepts, revolutionizing cell size limitations for many gas detector applications. The high radiation resistance and excellent spatial and time resolution make them an invaluable tool to confront future detector challenges at the next generation of colliders. The design of the new micro-pattern devices appears suitable for industrial production. Novel structures where MPGDs are directly coupled to the CMOS pixel readout represent an exciting field allowing timing and charge measurements as well as precise spatial information in 3D. Originally developed for the high energy physics, MPGD applications has expanded to nuclear physics, UV and visible photon detection, astroparticle and neutrino physics, neutron detection and medical physics.

1 Gaseous Detectors: Historical Overview

The single wire proportional counter, invented more 100 years ago by E. Rutherford and H. Geiger [1], and its high gain successor, the Geiger-Mueller counter first described in 1928 [2], can be considered the ancestors of all modern gaseous detectors and were for many decades a major tool for the study of ionizing radiation. Forty years ago, in 1968, the instrumentation in experimental particle physics was revolutionized with the advent of the Multi-Wire Proportional Chamber (MWPC) [3]. With its excellent accuracy and modest rate capability, the MWPC allowed large detector areas to be instrumented with fast tracking detectors and were able to localize particle trajectories with sub-mm precision. Confronted by the increasing demands of particle physics

[a] Invited Lectures at the Trans-European School of High Energy Physics, Zakopane, Poland, July 8-14 (2009); http://events.lal.in2p3.fr/TESchool09/

experiments, MWPCs have continuously improved over the years [4,5,6,7,8]. Gradually replacing slower detectors, numerous generations of gaseous devices, with novel geometries and exploiting various gas properties, has been developed: Drift Chamber [9], Multi-Drift Module [10], JET Chamber [11], Time Projection Chamber (TPC) [12], Time Expansion Chamber [13], Multi-Step Chamber [14], Ring-Imaging Cherenkov Counter [15] and many others. However, limitations have been reached in maximum rate capability and detector granularity. A fundamental rate limitation of wire chambers, due to positive ion accumulations, was overcome with the invention of Micro-Strip Gas Chamber (MSGC) [16], capable of achieving position resolution of few tens of microns at particle fluxes exceeding MHz/mm^2 [17]. Developed for the projects at high-luminosity colliders, MSGC's filled a gap between the performing but expensive solid-strip detectors and cheap but rate-limited traditional wire chambers. Despite their impressive performance, detailed studies of long-term behavior at high rates have revealed two possible weaknesses of the MSGC technology: a slow degradation under sustained irradiation (aging), and appearance of rare but destructive discharges in presence of highly ionizing particles [18].

The invention of Micro-Pattern Gas Detectors (MPGD), in particular the Gas Electron Multiplier (GEM) [19], the Micro-Mesh Gaseous Structure (Micromegas) [20], and other micro pattern detector schemes, offers the potential to develop new gaseous detectors with unprecedented spatial resolution, high rate capability, large sensitive area and operational stability [21,22]. Recent developments in radiation hardness research with state-of-the-art MPGD's revealed that they might be even less vulnerable to radiation-induced performance degradation than standard silicon micro-strip detectors [23,24]. In some applications, requiring very large-area coverage with moderate spatial resolutions, more coarse macro-patterned detectors, e.g. thick-GEMs (THGEM) [25,26,27] or patterned resistive thick GEM devices (RETGEM) [28] could offer an interesting and economic solution. In addition, the availability of highly integrated amplification and readout electronics allows for the design of gas-detector systems with channel densities comparable to that of modern silicon detectors. An elegant solution is the use of a CMOS pixel ASIC[b], assembled directly below the GEM or Micromegas amplification structures [29,30,31,32]. Modern wafer post-processing also allows for the integration of Micromegas grid directly on top of a CMOS pixelized readout chip [33]. In 2008, the RD51 collaboration at CERN has been established to further advance technological developments of micro-pattern gaseous detectors and associated electronic-readout systems, for applications in basic and applied research [34].

2 Basic Principles: Ionization, Transport Phenomena and Avalanche Multiplication

The process of detection in gas proportional counters starts with the inelastic collisions between the incident particles and gas molecules. These collisions lead to excitation of the medium (followed by the emission of the light, the basis of scintillation detectors) and ionization, the primary signal for tracking devices. The number N_P and the space distribution of the primary ionization clusters depend on the nature and energy of the radiation. The primary electrons can often have enough energy to further ionize the medium; the total number of electron-ion pairs (N_T) is usually a few times larger than the number of primaries (N_P). Table 1 provides values of relevant parameters in some commonly used gases at NTP (normal temperature and pressure) for unit charge minimum-ionizing particles (MIPs)[35]. Values often differ, depending on the source, and those in the table should be taken only as approximate.

The primary statistics determines several intrinsic performances of gas detectors, such as efficiency, time resolution and localization accuracy. The actual number of primary interactions follows the Poisson's statistics; the inefficiency of a perfect detector with a thin layer of gas is

[b] Application Specific Integrated Circuit

Table 1: Properties of noble and molecular gases at normal temperature and pressure (NTP: 20° C, one atm). E_X, E_I: first excitation, ionization energy; W_I: average energy per ion pair; $dE/dx|_{\min}$, N_P, N_T: differential energy loss, primary and total number of electron-ion pairs per cm, for unit charge minimum ionizing particles.

Gas	Density mg cm^{-3}	E_x eV	E_I eV	W_I eV	$dE/dx\|_{\min}$ keV cm^{-1}	N_P cm^{-1}	N_T cm^{-1}
He	0.179	19.8	24.6	41.3	0.32	3.5	8
Ne	0.839	16.7	21.6	37	1.45	13	40
Ar	1.66	11.6	15.7	26	2.53	25	97
Xe	5.495	8.4	12.1	22	6.87	41	312
CH_4	0.667	8.8	12.6	30	1.61	28	54
C_2H_6	1.26	8.2	11.5	26	2.91	48	112
iC_4H_{10}	2.49	6.5	10.6	26	5.67	90	220
CO_2	1.84	7.0	13.8	34	3.35	35	100
CF_4	3.78	10.0	16.0	54	6.38	63	120

given by exp(-N_P). For example, in one mm of Ar/CO_2 (70:30) approximately 6 % of all MIPs do not release a single primary electron cluster and therefore can not be detected. The total energy loss, sum of primary and secondary ionization, follows a statistical distribution described by a Landau function, with characteristic tails towards higher values. A simple composition law can be used for gas mixtures: for example, the number of primary (N_P) and total (N_T) electron-ion pairs produced by MIP in a 1 cm of Ar/CO_2 (70:30) mixture at NTP:

$$N_P = 25 \cdot 0.7 + 35 \cdot 0.3 = 28 \ \frac{pairs}{cm}; \quad N_T = \frac{2530}{26} \cdot 0.7 + \frac{3350}{35} \cdot 0.3 \approx 97 \ \frac{pairs}{cm} \qquad (1)$$

While charged particles release ionization trail of primary electron clusters, low energy X-rays undergo a single localized interaction, usually followed by the emission of the photo-electron, accompanied by the lower-energy photon or Auger electron. For example, a 5.9 keV X-ray converts in argon mainly on a K shell (3.2 keV); the emitted photo-electron with energy $E_\gamma - E_K \sim 2.7$ keV has a practical range in detector of ~ 200 μm. In addition, with 85 % probability another (Auger) electron with energy ~ 3.2 keV (~ 250 μm range in argon) is ejected; in the remaining cases, a 3 keV K-L fluorescence photon is produced with a mean absorption length of 40 mm. The sum of the energies of photo-electron and Auger electron is responsible for the main 5.9 keV peak, while fluorescence mechanism leads to the Ar escape peak. The total number of electron-ion pairs created by X-ray absorbed in argon can be evaluated by dividing its energy by the W_I: $\frac{5900}{26} \approx 227$.

Once released in the gas, and under the influence of an applied electric field, electrons and ions drift in opposite directions and diffuse towards the electrodes. When electron move through the gas, the magnitude of the scattering cross section in an electron-atom (molecule) collision is determined by the details of atomic and molecular structure. Therefore, the drift velocity and diffusion of electrons depend very strongly on the nature of the gas, namely on the structure of inelastic cross-section, arising from rotational and vibrational levels of molecules. In noble gases, the inelastic cross section is zero below excitation and ionization thresholds. Large drift velocities are achieved by adding polyatomic gases (usually CH_4, CO_2 or CF_4), having large inelastic cross sections at moderate energies, which results in "cooling" electrons into an energy range of the Ramsauer-Townsend minimum (located at ∼0.5 eV) of the momentum transfer elastic cross-section of argon. The reduction in both the total electron scattering cross-section and the electron energy results in a large increase of electron drift velocity (for a compilation of electron-molecule cross sections see Ref. [36]). Another principal role of the polyatomic gas is to absorb

the ultraviolet (UV) photons emitted by the excited inert gas atoms. The quenching of UV photons occurs through the photo-decomposition of polyatomic molecules. Extensive collections of experimental data[37] and theoretical calculations based on transport theory[38] permit estimates of drift and diffusion properties in pure gases and their mixtures. In a simple approximation, gas kinetic theory provides the following relation between drift velocity, v, and the mean collision time between electron and molecules, τ (Townsend's expression): $v = eE\tau/m$. Values of drift velocity and diffusion for some commonly used gases at NTP are given in Fig. 1a and Fig. 1b. These have been computed with the MAGBOLTZ program[39]. Using fast CF_4-based mixtures at fields around kV/cm^{-1}, the electron drift velocity is around 10 $cm \cdot \mu s^{-1}$ and the corresponding drift time 100 $ns{\cdot}cm^{-1}$. For different conditions, the horizontal axis must be scaled inversely with the gas pressure or density, $1/P$, where P is the pressure. Standard deviations for longitudinal (σ_L) and transverse diffusion (σ_T) are given for one cm of drift, and scale with the square root of distance. Since the collection time is inversely proportional to the drift velocity, diffusion is smaller in gases having large drift velocities, such as for CF_4. In the presence of an external magnetic field, the Lorentz force acting on electrons between collisions deflects the drifting electrons and modifies the drift properties. For parallel electric and magnetic fields, drift velocity and longitudinal diffusion are not affected, while the transverse diffusion can be strongly reduced: $\sigma_T(B) = \sigma_T(B=0)/\sqrt{1+\omega^2\tau^2}$. The dotted line in Fig. 1b represents σ_T for the classic Ar/CH_4 (90:10) mixture at 4 T. This reduction is exploited in TPC to improve spatial resolution.

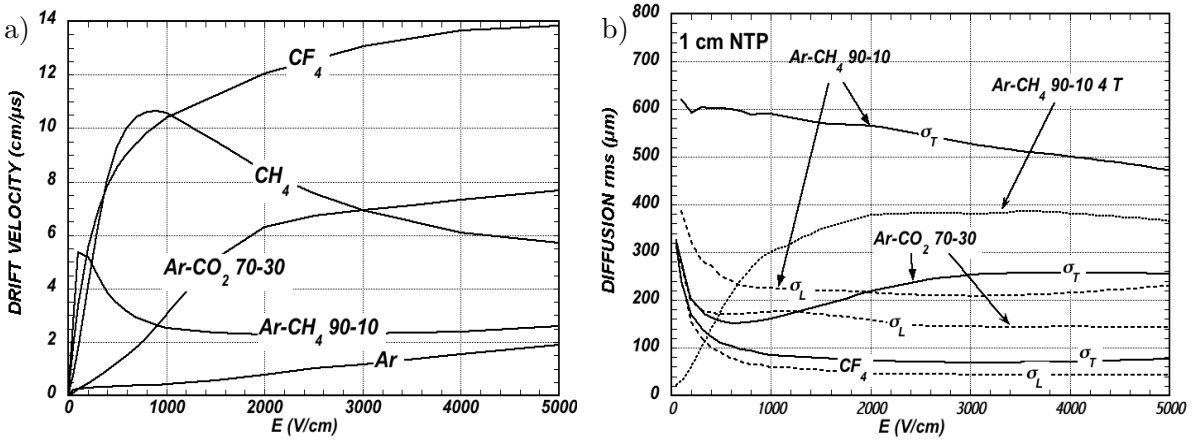


Figure 1: a) Computed electron drift velocity with the MAGBOLTZ program as a function of electric field in several gases at NTP and B=0. b) Electron longitudinal diffusion (σ_L) (dashed lines) and transverse diffusion (σ_T) (full lines) for 1 cm of drift at NTP and B = 0. The dotted line shows σ_T for the Ar/CH_4(90:10) gas at 4T.

In mixtures containing electronegative molecules such as O_2, H_2O or CF_4, electrons can be captured to form negative ions. Capture cross-sections are strongly energy-dependent, and therefore the capture probability is a function of applied field. For example, the electron is attached to the oxygen molecule at energies below 1 eV, while dissociative electron attachment to the CF_4 occurs mainly in the 6 to 8 eV range [40]. The three-body electron attachment coefficients may differ greatly for the same addition in different mixtures. As an example, at moderate fields (up to 1 kV/cm) the addition of 0.1% of oxygen to an Ar/CO_2 mixture results in an electron capture probability about twenty times larger than the same addition to Ar/CH_4.

The primary ionization signal is very feeble in a gas layer: in one cm of Ar/CO_2 (70:30) at NTP around ~ 100 electron-ion pairs are created (see Eq. 1). Therefore, one has to use "internal gas amplification" mechanism to generate detectable signal in gas counters; excitation and subsequent photon emission participate in the avalanche spread processes and can be also detected by optical means. If the electric field is increased sufficiently, electrons gain enough energy between collisions to undergo inelastic collisions with gas molecules. Above a gas-dependent threshold, the mean free path for ionization, λ_i, decreases exponentially with the field; its inverse, $\alpha = 1/\lambda_i$,

is the first Townsend coefficient. In single wire proportional counter, most of the increase of avalanche particles occurs very close to the anode wires, and a simple electrostatic consideration shows that the largest fraction of the detected signal is due to the motion of positive ions receding from the wires. The electron component, although very fast, contributes very little to the signal. This determines the characteristic shape of the detected signals in the proportional mode: a fast rise followed by a gradual increase. The slow component, the so-called "ion tail" that limits the time resolution of the counter, is usually removed by differentiation of the signal. In uniform fields, N_0 initial electrons multiply over a length x forming an electron avalanche of size $N = N_0\, e^{\alpha x}$; N/N_0 is the gain of the counter. With present-day electronics, proportional gains around $5 \cdot 10^3 - 10^4$ are sufficient for detection of minimum ionizing particles, and noble gases with moderate amounts of polyatomic gases, such as methane or carbon dioxide, are used.

Positive ions released by the primary ionization or produced in the avalanches drift and diffuse under the influence of the electric field. Negative ions may also be produced by electron attachment to gas molecules. The drift velocity of ions in the fields encountered in gaseous counters (up to few kV/cm) is typically about three orders of magnitude lower than for electrons. The ion mobility, μ, the ratio of drift velocity to electric field, is constant for a given ion type up to very high fields [41,42]. For mixtures, due to a very effective charge transfer mechanism, only ions with the lowest ionization potential survive after a short path in the gas. The diffusion of ions, both σ_L and σ_T, are proportional to the square root of the drift time, with a coefficient that depends on temperature but not on the ion mass. Accumulation of ions in the gas volume may induce gain reduction and field distortions.

3 The Multi-Wire Proportional, Drift and Time Projection Chambers

The invention of the Multi-Wire Proportional Chambers (MWPC) revolutionized the field of radiation detectors [3,5]. In the original design, the MWPC consists of a set of parallel, evenly spaced, anode wires stretched between two cathode planes. Applying potential difference between anodes and cathodes, field lines and equipotentials develop as shown in Fig. 2a. Electrons released in the gas volume drift towards the anodes and produce avalanche in the increasing field. Typical values for the anode wire spacing range between 1 and 5 mm, the anode to cathode distance is 5 to 10 mm. The operation gets increasingly difficult at smaller wire spacings, which prevented taking this direction for obtaining higher spatial resolution. For example, the electrostatic repulsion for thin (10 μm) anode wires causes mechanical instability above a critical wire length, which is less than 25 cm for 1-mm wire spacings. The signal multiplication process, which begins a few radii from the anode, is over after a fraction of nanosecond, leaving the cloud of positive ions receding from the anode. Detection of charge on the anode wires over a predefined threshold provides the transverse coordinate to the wire with an accuracy comparable to that of the wire spacing. With a digital readout and $s = 1$ mm wire spacing, the spatial resolution is limited to: $\sigma = \frac{s}{\sqrt{12}} = 300$ μm. The coordinate along each wire can be obtained by measuring the ratio of collected charge at the two ends of resistive wires. The slow motion of positive ions produced in the avalanche is responsible for the largest fraction of charge signals detected on all surrounding electrodes; a measurement of the charge profile induced on segmented cathodes, allows bi-dimensional localization of the ionizing event. This is the so-called center-of-gravity (COG) method, which permits to attain the highest localization accuracy in MWPCs. Due to the statistics of energy loss and asymmetric ionization clusters, the position accuracy is ~ 50 μm rms for tracks perpendicular to the wire plane, but degrades to ~ 250 μm at 30° to the normal [43].

Drift chambers, developed in the early '70's, can estimate the position of a track by exploiting the arrival time of electrons at the anodes if the time of interaction is known [9]. The distance between anode wires is usually several cm allowing coverage of large areas at reduced cost. Many

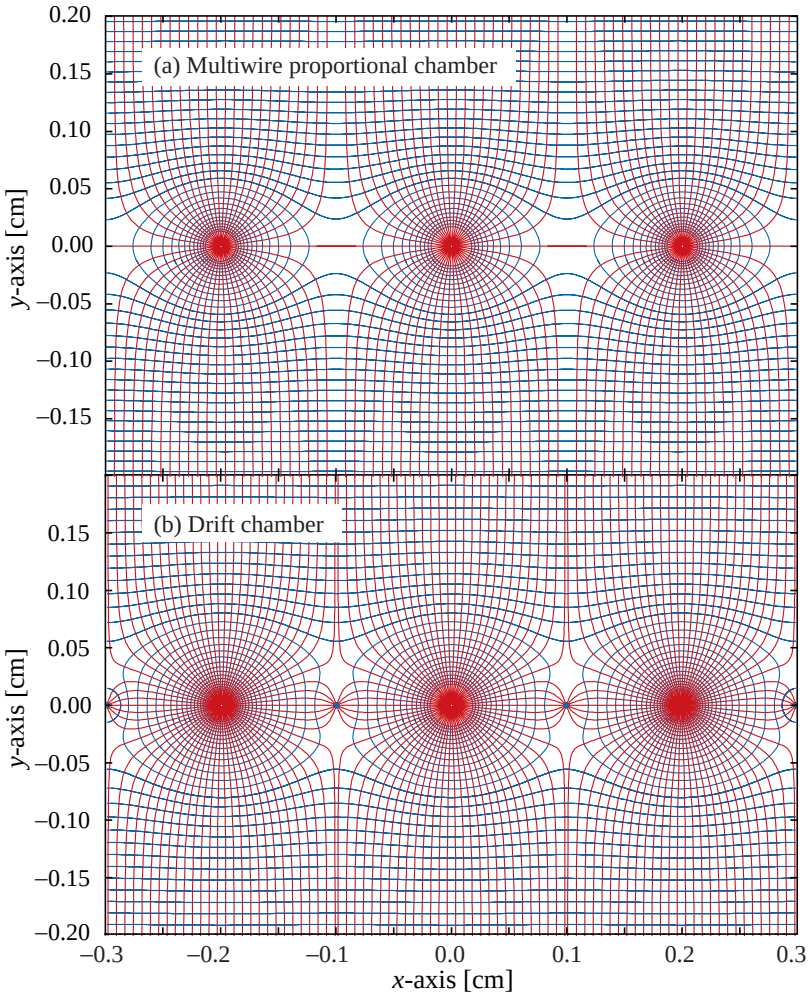


Figure 2: Electric field lines and equipotentials in (a) a multiwire proportional chamber and (b) a drift chamber. Thin anodes wires between two cathodes acts as a set of independent proportional counters.

designs have been introduced aimed at improving performance. In the original design, a thicker wire at proper voltage between anodes (field wire) reduces the field at the middle point between anodes, improving charge collection (Fig. 2b). In some drift chambers design, and with the help of suitable voltages applied to field-shaping electrodes, the electric field structure is adjusted to improve the linearity of space-to-drift-time relation, resulting in better spatial resolution [44]. Drift chambers can reach a spatial resolution from timing measurement of order 100 μm (rms) or better for minimum ionizing particles, depending on geometry and operating conditions. A degradation of resolution is observed however for tracks close to the anode wires, caused by the spread in arrival time of the nearest ionization clusters, due to primary ionization statistics [45]. Sampling the drift time on rows of anodes led to the concept of multiple arrays such as the multi-drift module [10] and the JET chamber [11]. A measurement of drift time, together with the recording of charge sharing from the two ends of the anode wires provides the coordinates of segments of tracks; the total charge gives information on the differential energy loss and is exploited for particle identification.

The "ultimate" drift chamber is the TPC concept invented in the 1976 [12], which combines a measurement of drift time and charge induction on cathodes to obtain excellent tracking for high multiplicity topologies occurring at moderate rates. It has been the prime choice for large tracking systems in e^+e^- colliders (PEP-4 [46], ALEPH [47], DELPHI [48]) and proved its unique resolving power in the heavy ion collisions (NA49 [49], STAR [50]). A TPC consists of a large gas volume, with an uniform electric field applied between the central electrode and a grid at

the opposite side. The ionization trails produced by charged particles drift towards the readout end-plate, where a 2D image of tracks is reconstructed; the third coordinate is measured using the drift time information. In all cases, a good knowledge of electron drift velocity and diffusion properties is required. This has to be combined with the 3D modeling of electric fields in the structures, computed with commercial or custom-developed software [39,51]. Conventional readout structure, based on MWPC and pads, is a benchmark for the "most modern" ALICE TPC, designed to cope with extreme instantaneous particle densities produced in heavy ion collisions at the LHC. This detector incorporates innovative and state of the art technologies, from the mechanical structures to the readout electronics and data processing chain [52]. To limit distortions to the ALICE TPC intrinsic spatial resolution ($\sigma_{r\phi}$ ~1000 μm for 250 cm drift length), the temperature gradient in a 88 m^3 gas volume space must not exceed $0.1°C$ [53]. For an overview of detectors exploiting the drift time for coordinate measurement see Ref. [7] and Ref. [8].

Despite various improvements, position-sensitive detectors based on wire structures are limited by basic diffusion processes and space charge effects in the gas to localization accuracies around 100 μm[54]. The presence of slow moving positive ions from electron avalanches generates a positive space charge in the drift tube, that modifies electric field and leads to the uncertainty in the space-to-drift time relation. In standard operating conditions, the gain of a MWPC starts to drop at particle rates above 10^4 $mm^{-2}s^{-1}$, leading to a loss of detection efficiency [44] (see Fig. 3). Together with the practical difficulty to manufacture detectors with sub-mm wire spacing, this has motivated the development of new generation gaseous detectors for high luminosity accelerators.

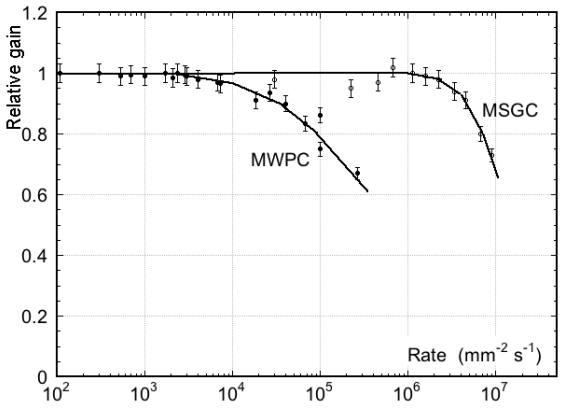


Figure 3: Normalized gas gain as a function of particle rate for Multi-Wire Proportional Chamber (MWPC) and Micro-Strip Gas Chamber (MSGC).

4 Micro-Pattern Gas Detectors (MPGD)

Modern photo-lithographic technology led to the development of novel Micro-Pattern Gas Detector (MPGD) concepts [5], revolutionizing cell size limitations for many gas detector applications. By using pitch size of a few hundred microns, an order of magnitude improvement in granularity over wire chambers, these detectors offer intrinsic high rate capability ($> 10^6$ Hz/mm^2), excellent spatial resolution ($\sim$ 30 μm), multi-particle resolution ($\sim$ 500 μm), and single photo-electron time resolution in the ns range.

The Micro-Strip Gas Chamber (MSGC), a concept invented in 1988, was the first of the micro-structure gas detectors[16]. It consists of a set of tiny parallel metal strips laid on a thin resistive support, alternatively connected as anodes and cathodes (see Fig. 4a). The principle of MSGC resembles a multi-anode proportional counter, with fine printed strips instead of wires,

see Fig. 4b. Owing to the small anode-to-cathode distance ($\sim 100\ \mu m$), the fast collection of positive ions by nearby cathode strips reduces space charge build-up, and pushes the maximum rate capability of MSGC, compared to MWPC, by more than two orders of magnitude [17] (see Fig. 3). Despite their promising performance, experience with MSGCs has raised serious concerns about their long-term behavior. There are several major processes, particularly at high rates, leading to the MSGC operating instabilities: substrate charging-up and time-dependent modification of electric field, surface deposition of polymers (aging) and destructive micro-discharges under exposure to heavily ionizing particles [5,55]. The problem of discharges is the intrinsic limitation of all single-stage micro-pattern detectors in hadronic beams [56,57,58]. Whenever the total charge in the avalanche exceeds a value of $10^7 - 10^8$ electron-ion pairs (Raether limit), an enhancement of the electric field in front of and behind the primary avalanche induces the fast growth of a filament-like streamer followed by breakdown. This has been confirmed under a wide range of operating conditions and multiplying gaps [59,60,61,62]. In the high fields and narrow gaps, the MSGC turned out to be prone to irreversible discharges induced by heavily ionizing particles and destroying the fragile electrode structure [18] (see Fig. 4c). Nevertheless, the detailed studies on their properties, and in particular, on the radiation-induced processes leading to discharge breakdown, led to the development of mature technologies and novel approaches (GEM and Micromegas) with similar performances, improved reliability and radiation hardness. The MPGD structures can be grouped in two large families: micromesh-based detectors and hole-type structures. The micromesh-based structures include: Micromegas, "Bulk" Micromegas, "Microbulk" Micromegas and "InGrid". The Hole-type structures are: GEMs, THGEM, RETGEM and Micro-Hole and Strip Plate (MHSP) elements.

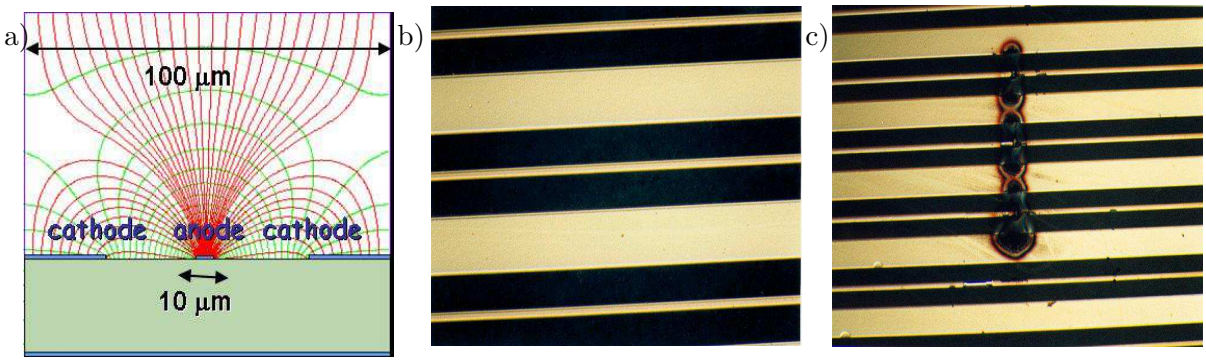


Figure 4: a) Schematic view, equipotentials and field lines in the MSGC; b) Microscopic image of the MSGC. On an insulating substrate, thin metallic anode strips alternate with wider cathodes; the pitch is 200 μm; c) Image of MSGC electrodes damaged by discharge. The very thin metal layers of MSGCs (few hundred nanometers) makes them vulnerable for discharges, which can easily destroy fragile structure.

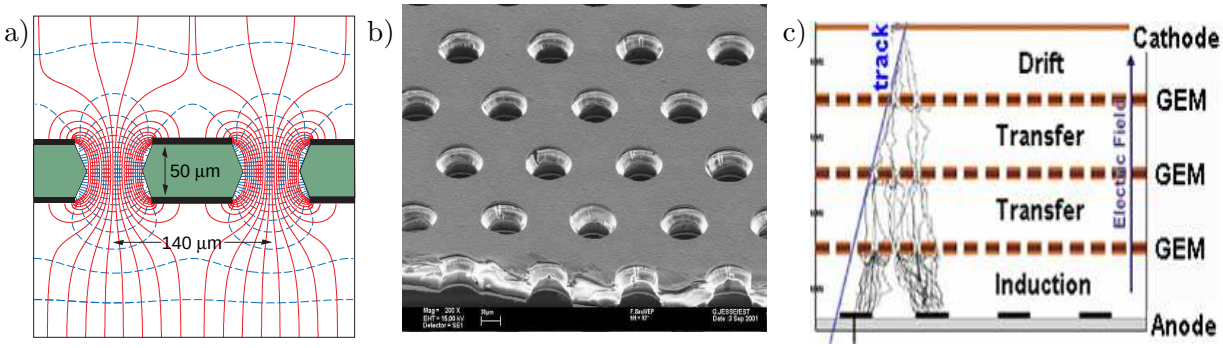


Figure 5: a) Schematic view and typical dimensions of the hole structure in the GEM amplification cell. Electric field lines (solid) and equipotentials (dashed) are shown; b) Electron microscope view of a GEM foil etched on a copper-clad, 50 μm thick polymer foil. The hole's diameter and pitch are 70 μm and 140 μm; c) Schematic view of the triple-GEM detector.

Introduced in 1996 by F. Sauli [19], a Gas Electron Multiplier (GEM) detector consists of a thin-foil copper-insulator-copper sandwich chemically perforated to obtain a high density of holes. The GEM manufacturing method, developed at CERN, is a refinement of the double-side printed circuit technology. The hole diameter is typically between 25 μm and 150 μm, while the corresponding distance between holes varies between 50 μm and 200 μm. The central insulator is usually (in original design) the polymer kapton, with a thickness of 50 μm (see Fig. 5b). Controlled etching of GEM foils (decreasing the thickness of the copper layer from 5 to 1 μm) allows to reduce material budget in triple-GEM to $1.5\times10^{-3}X_0$, which is about one half of a 300-μm-thick Si-microstrip detector [63]. Application of a potential difference between the two sides of the GEM generates the electric fields indicated in Fig. 5a. Each hole acts as an independent proportional counter. Electrons released by the primary ionization particle in the upper conversion region (above the GEM foil) drift into the holes, where charge multiplication occurs in the high electric field (50 - 70 kV/cm). Most of avalanche electrons are transferred into the gap below the GEM [64,65]. Several GEM foils can be cascaded (see Fig. 5c), allowing the multi-layer GEM detectors to operate at overall gas gain above 10^4 in the presence of highly ionizing particles, while strongly reducing the risk of discharges ($< 10^{-12}$ per hadron) [66,67]. This is a major advantage of the GEM technology. A unique property of GEM detector is a full decoupling of the amplification stage (GEM) and the readout electrode (PCB), which operate at unity gain and serves only as a charge collector. Localization can then be performed by collecting the charge on a one- or two-dimensional readout board of arbitrary pattern, placed below the last GEM. The signal detected on the PCB is entirely due to the electron collection, without a slow ion tail, and is typically few tens of nanosecond for 1 mm-wide induction gap. Cascaded GEMs reach gains above 10^5 with single electrons; this permitted conceiving gaseous imaging photo-multipliers (GPM) with single photon sensitivity [68]. Moreover, with an appropriate choice of GEM fields and geometry, both photon and ion feedback can be considerably suppressed.

The MHSP is a GEM-like hole-electrode with anode- and cathode-strips etched on the bottom face of the GEM; the avalanche developed inside the hole is further multiplied on the anode strips [69]. When operating the MHSP and biasing the strips in reverse mode, i.e. using an extra electrode to attract positive ions, a breakthrough in ion blocking capability has been achieved in MHSP/GEM cascaded multipliers [70].

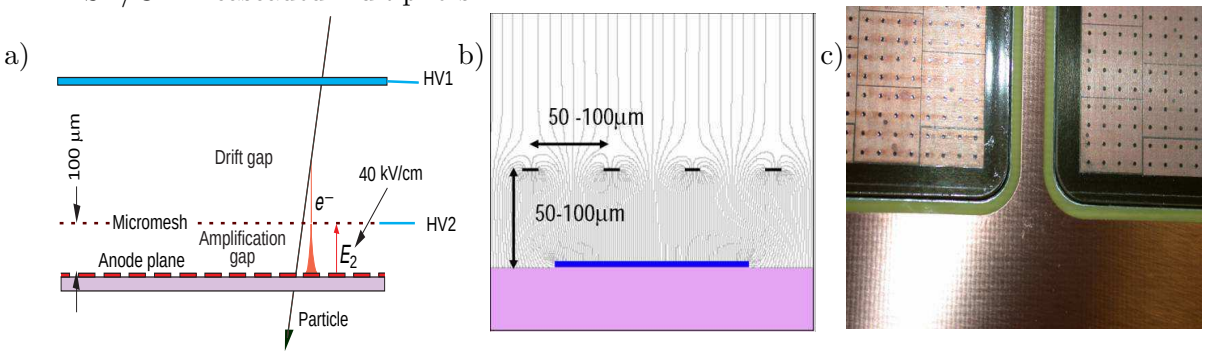


Figure 6: a) Schematic view of the Micromegas detector (not to scale). A few mm drift gap is between the cathode electrode and micromesh, and the 100 μm amplification gap is defined by the micromesh and the anode strip readout; b) Electric field map in Micromegas. A metallic micromesh separates a low-field ($\sim 1\ kV/cm$) drift region from the high-field multiplication region ($\sim 40 - 80\ kV/cm$). c) Photograph of the "Bulk" Micromegas detectors. Pillars of 400 μm diameter every 2 mm are visible.

Introduced in 1996 by Y. Giomataris, the Micromegas is a thin parallel-plate avalanche counter, as shown in Fig. 6a [20]. It consists of a few mm drift region and a narrow multiplication gap (25-150 μm) between a thin metal grid (micromesh) and the readout electrode (strips or pads of conductor printed on an insulator board). To preserve a distance between the anode and the micromesh, regularly spaced pillars from insulating material are used. Electrons from the

primary ionization drift through the holes of the mesh into the narrow multiplication gap, where they are amplified. The electric field is homogeneous both in the drift (electric field ∼1 kV/cm) and amplification (∼40-80 kV/cm) gaps (see Fig. 6b). Due to the narrow multiplication region, small variations of the amplification gap are counteracted by an inverse variation of the Townsend coefficient, thus improving the uniformity and stability of response over a large area [71]. Positive ions are quickly removed by the micromesh; this prevents space-charge accumulation and induces very fast signals with only a small ion tail, 50 - 100 ns length. The Micromegas retains the rate capability and energy resolution of the parallel-plate counter. The small amplification gap is a key element in Micromegas operation, giving rise to excellent spatial resolution: 12 μm accuracy, limited by the micromesh pitch, has been achieved for MIPs [72], a very good energy resolution (∼11% FWHM with 8 keV X-rays) [73] and single photo-electron time resolution better than 1 ns[74]. Efforts have been focused on producing the Micromegas amplification region as a single piece using the newly developed "Bulk" method [75]. A woven mesh is laminated on a PCB covered by a photo-imageable polyimide film, and the pillars are made by a photochemical technique with insulation through the grid. Such a "all-in-one" detector, called "Bulk" Micromegas, is robust and allows the regular production of large, stable and unexpensive detector modules. Fig. 6c shows photo of the large "Bulk" Micromegas (36*34 cm^2 active area) produced for the T2K TPC [76]. A new Micromegas manufacturing technique, based on kapton etching technology, has been recently developed, resulting in further improvement of the detector characteristics, such as flexible structure, low mass, high radio-putiry, uniformity and stability [77]. Excellent energy resolution has been obtained, reaching 11 % FWHM for the 5.9 keV X-rays and 1.8 % FWHM of the 5.5 MeV α-peak for the Am^{241} source.

The success of GEMs and glass capillary plates triggered the development of coarse and more robust structures, "optimized GEM" [25,78] followed by THGEM [26,27,79] gaseous multiplier. These are produced by standard printed circuit technology: mechanical drilling of 0.3-1 mm diameter holes, etched at their rims to enhance high-voltage stability (see Fig. 7a and 7b); different PCB materials can be used, of typical thicknesses of 0.4-1 mm and hole spacing of 0.7-1.2 mm. These electron multipliers exhibit specific features: the geometrical parameters can be scaled from GEM ones, but the microscopic behavior of the electrons, in particular diffusion in the gas, does not scale. The electron collection and transport between cascaded elements is more effective than in GEM because the THGEM's hole diameter is larger than the electron's diffusion range when approaching the hole. The THGEM detectors have been studied in laboratory, also in gaseous-photomultiplier configurations - coupled to semitransparent or reflecting CsI photo-cathodes (see Fig. 7a) [80]. Effective gas amplification factors of 10^5 and 10^7 can be reached in single and cascaded double-THGEM elements, which permits efficient imaging of light at single-photon level [79]. Stable operation at photon fluxes exceeding 1 MHz/mm^2 was recorded together with sub-mm localization accuracy and timing in the 10 ns range [27,81].

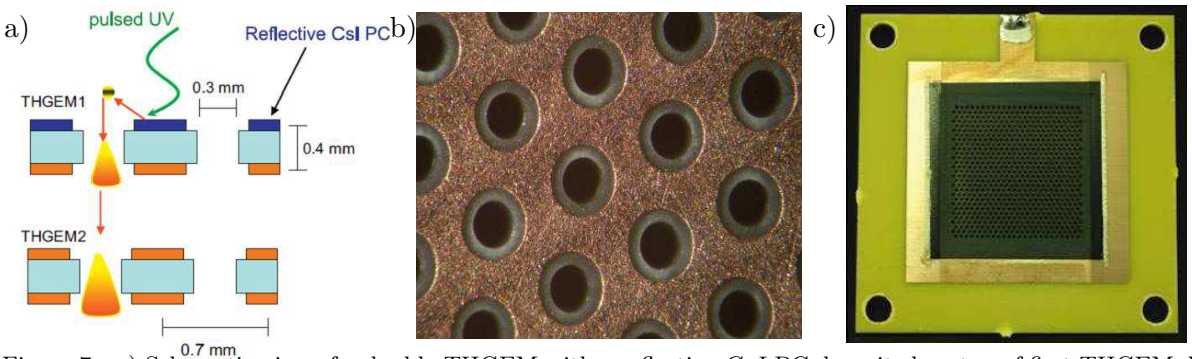


Figure 7: a) Schematic view of a double-THGEM with a reflective CsI PC deposited on top of first THGEM; b) Photo of the Thick GEM (THGEM) multiplier. A rim of 0.1 mm is chemically etched around the mechanically drilled holes to reduce discharges; c) Photo of the RETGEM detector with resistive kapton electrodes.

A novel spark-protected version of thick GEM with resistive electrodes (RETGEM) has been recently developed, where the Cu-clad conductive electrodes are replaced by resistive materials [82,83,84]. Sheets of carbon loaded kapton 50 μm thick or screen-printed resistive surface are attached onto both surfaces of the PCB to form resistive-electrode structure; holes 0.3 mm in diameter with a pitch of 0.6 mm are mechanically drilled (see Fig. 7b). At low counting rates, the detector operates as a conventional THGEM with metallic electrodes, while at high intensities and in case of discharges the behavior is similar to a resistive-plate chamber.

5 Micro-pattern Gas Detector Applications

The performance and robustness of MPGDs have encouraged their use in high-energy and nuclear physics, UV and visible photon detection, astroparticle and neutrino physics, X-ray imaging and neutron detection and medical physics. Common themes for future applications are low mass, large active areas, high spatial resolution, high rate capabilities and high radiation tolerance.

Due to the wide variety of geometries and flexible operating parameters, MPGDs are a common choice for tracking and triggering detectors in nuclear- and particle-physics. COMPASS, a high-luminosity experiment at CERN, pioneered the use of large-area ($\sim 40 \times 40$ cm^2) GEM and Micromegas detectors close to the beam line with particle rates of 25 kHz/mm^2. Both technologies achieved a tracking efficiency of close to 100% at gas gains of about 10^4, a spatial resolution of 70–100 μm and a time resolution of $\sim$ 10 ns [85,86]. For the future COMPASS physics program, a set of Micromegas detectors with pixelized readout in the central region is being proposed [87]. High resolution planar triple-GEM detectors are used in the LHCb Muon System [88], for the TOTEM Telescopes [89] and also being developed for PANDA experiment at the future FAIR facility [90], SBS spectrometer for Hall A at Jefferson lab [91], and as a forward Tracker of STAR experiment at RHIC [92]. Using fast CF_4-based mixtures, a time resolution of about 5 ns rms is achieved [93], adequate to resolve two bunch crossings at the Large Hadron Collider (LHC). Therefore, large area MPGDs are currently being considered for the LHC machine upgrade program (sLHC), aiming to increase the luminosity by a factor of ~ 10, as a potential replacement of conventional gaseous detectors. Micromegas coupled to the CMOS readout may be employed as new vertex detector system at the sLHC [94]. GEMs and Micromegas can be also bent to form cylindrically curved ultra-light detectors, as preferred for inner tracker (barrel) and vertex applications [95,96].

For the future International Linear Collider applications, both GEM and Micromegas devices are foreseen as one of the main options for the TPC [97,98,99]. Compared to wire chambers, they offer number of advantages: negligible E×B track distortion effects, the narrow pad response function (PRF) and the intrinsic suppression of ion back-flow, relaxing the requirements on gating of the devices and, depending on the design, possibly allowing non-gated operation of TPCs. Large-area MPGD systems are also being studied as a potential solution for highly granular digital hadron calorimeter. Implementations in GEM [100], Micromegas [101], and THGEM technologies have been proposed.

In the recent years there has been a considerable progress in the field of gaseous photomultipliers by combining MPGD with semi-transparent or reflective CsI-photocathodes (PC) to localize single photoelectrons [102,103,104]. The operation of MPGD-based photomultipliers in CF_4 with CsI-PC could form the basis of new generation windowless Cherenkov detectors, where both the radiator and the photosensor operate in the same gas. Exploiting this principle, originally proposed for Parallel Plate Avalanche Chamber [105], a Hadron Blind Detector was successfully operated using triple-GEM amplification system with CsI-PC for the PHENIX experiment at RHIC [106,107]. A hadron-blindness property is achieved by reversing the direction of the drift field E_D, therefore pushing primary ionization produced by charged particles towards the mesh. In this configuration photoelectrons released from the CsI-PC surface are

still effectively collected into the GEM holes due to the strong electric field inside holes. For many applications in photon detectors, a rather coarse (sub-mm) spatial resolution is usually sufficient. Therefore THGEM and RETGEM are under study for RICH detector upgrades for COMPASS and ALICE [108].

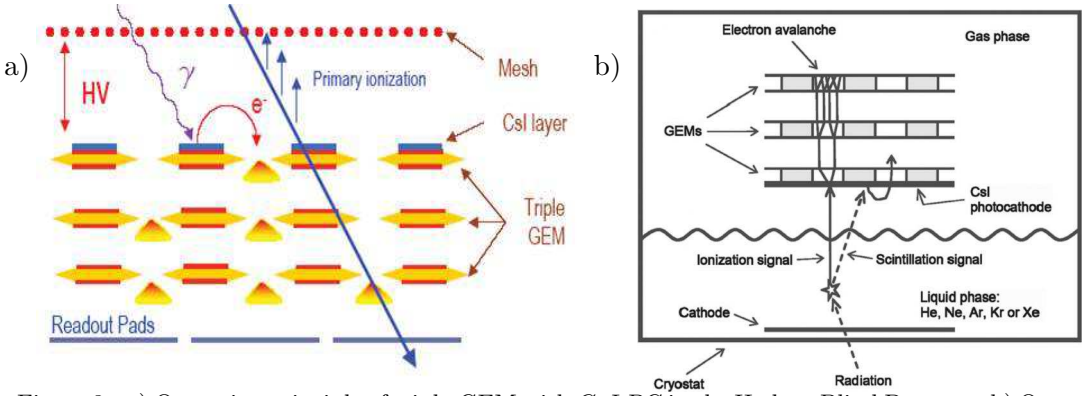


Figure 8: a) Operation principle of triple-GEM with CsI-PC in the Hadron Blind Detector; b) Operation principle of the two-phase avalanche detector with a triple-GEM and reflective CsI-PC; both ionization and scintillation signals from the liquid are detected.

Recent progress in the operation of cascaded GEM, Micromegas, THGEM and RETGEM GPMs at cryogenic temperatures (down to 80 K) [109] and in two-phase mode [110,111,112] could pave the road towards their potential applications for the next generation neutrino physics and proton decay experiments [113,114], direct dark matter searches [115], Positron Emission Tomography (PET) [116], and for noble-liquid Compton telescope, combined with a micro-PET camera [117,118]. The operation principle of the cryogenic two-phase avalanche detector with GEM readout is demonstarted in Fig. 8b: the ionization produced in the noble liquid by radiation is extracted from the liquid into the gas phase by an electric field. The multi-GEM detector, operated at cryogenic temperature in saturated vapor above the liquid phase, can detect both the ionization signal, extracted from the liquid, and the scintillation signal, generated in the noble liquid by a particle [111]. The latter is achieved by depositing an UV-sensitive photocathode, namely CsI, on top of the first GEM (see Fig. 8b). The detection of both scintillation and ionization signals could allows efficient background rejection in rare-event experiments; in PET applications, the detection of scintillation signals could provide a fast trigger for coincidences between two collinear gamma-quanta.

X-ray counting and imaging detectors, based on MPGDs, are being used for diffraction experiments at synchrotron radiation facilities [119] and could serve as a powerful diagnostic tool for magnetic fusion plasmas [120]. An innovative GEM-based system, which combines fast imaging of X-ray emissions with spectral resolution in the VUV range (0.2-10 keV), has been developed to study 2D dynamics of plasma instabilities and to control core plasma position, both being crucial issues for fusion researches [120]. Another recent development is the construction of the spherical GEM detector for parallax-free X-ray diffraction measurements, produced by the CERN/RD51 group in collaboration with industry [121]. In the rare-event experiments, MPGDs are used in searching for solar axions (CAST), where the expected signal comes from solar axions conversions into low-energy photons of 1-10 keV range. Micromegas with high granularity anode elements can largely reduce the background event rate down to $5\times10^{-5}\mathrm{keV}^{-1}\mathrm{cm}^{-2}\mathrm{s}^{-1}$, exploiting its stability, good energy and spatial resolution [122].

There are many applications of the Micromegas in the neutron detection domain, which include neutron beam diagnostics [123], inertial fusion experiments [124], thermal neutron tomography [125] and a sealed Picollo-Micromegas detector, designed to provide in-core measurements of the neutron flux and energy (from thermal to several MeV) in the nuclear reactor [126]. Neutrons can be converted into charged particles to detect ionization in Micromegas by two means:

either using the detector gas filling or target with appropriate deposition on its entrance window.

There were attempts to use GEM detectors for medical physics and portal imaging. In particular, GEM-based prototype was used to detect simultaneously the position of the therapeutic radiation beam (γ's) and the position of the patient tumor, using X-rays, in order to provide feedback to the cancer treatment machine and to correct on-line position of the beam with respect to the patient [127,128]. In this device, the X-ray image was obtained using conversions in gas and the γ-beam profile was determined using solid converters placed in between several GEM foils. Another medical application is the radiation therapy, which demands new on-line beam monitoring systems with ~ 1 mm spatial resolution and 3D dosimetry of delivered doses with an accuracy of 5 %. A scintillation light produced in the double-GEM detector during avalanche development was detected by commercial CCD camera. With a 360 MeV α-beam the scintillating GEM light signal at the Bragg peak was only 4 % smaller than of the reference ionization chamber. Consequently, GEM detector with CCD readout could become a feasible substitute for the Lanex scintillating screen, especially for α- or carbon-ion beams.

Finally, MPGDs can be used for a variety of security related applications: detection of dangerous cargo [130], radon detection in the air as an early warning of earthquakes [131] and UV sensitive early forest fire detection system [133,132]. Muon tomography, based on the measurement of multiple scattering of cosmic ray muons traversing cargo of vehicles that contain high-Z materials, is a promising passive interrogation technique to detect hidden nuclear materials. Large area GEM detectors for precise tracking of atmospheric muons in combination with affordable electronics and readout system is being developed by one of the RD51 collaborating institutes [130]. Among the planetary disasters the most common and often happening are the earthquakes and forest fires. A sharp increase in the Rn concentration before earthquakes has been observed in the air regions associate to rocks and caves and its detection can serve as a basis of an early earthquake warning system. The RETGEM-based device, capable to operate in the air and to continuously monitor the Rn concentration, is currently under development. A network of such detectors can installed in the sensitive regions to provide daily assessment of the Rn concentration [131]. The same RD51 group is also developing a RETGEM-based detector, which could be used for detection of forest fires at distances up to 1 km, compared with a range of 200 m for commercially available UV-flame devices [133,132].

6 Development of large area MPGDs

A big step in the direction of the industrial manufacturing of large-size MPGD's with size of few m^2 and spatial resolution typical of silicon micro-strip devices ($30 - 50$ μm) is the development of the new fabrication technologies - single mask GEM [134] and "Bulk" Micromegas [75]. Methods of their effective production and characterization are under investigation within the RD51 collaboration.

Recent developments on large area GEMs are focused on two new techniques to overcome the existing limitations: a single-mask technology and a splicing method for GEM foils [134]. The standard technique for creating the GEM hole pattern, involving accurate alignment of two masks, is replaced by a single-mask technology to pattern only the top copper layer. The bottom copper layer is etched after the polyamide, using the holes in the polyamide as a mask. A single mask technique overcomes the cumburstone practice of alignment of two masks between top and bottom films within 5-10 μm, which limits the achievable lateral size to ~ 50 cm. In a splicing procedure, foils are glued over a narrow seam, obtaining a larger foil. Both techniques were successfully implemented in the large-area prototype of 66×66 cm^2 size, produced in collaboration with CERN TS-DEM workshop, shown in Fig. 9a. Single mask GEM seems to be much more suitable for industrial large scale production than standard GEM technology.

The basic idea of the "Bulk" Micromegas technology is to built the whole detector in a single

process: the anode plane with copper strips, a photo-imageable polyamid film and the woven mesh are laminated together at a high temperature forming a single object [75]. At the end, the micromesh is sandwiched between two layers of insulating material, which is removed after UV exposure and chemical development. This "Bulk" Micromegas technique has been recently extended to produce large area prototypes in CERN TS-DEM workshop, up to 150×50 cm^2 in a single piece (see Fig. 9b) [135].

The THGEM and RETGEM technologies could offer economically interesting solution for a single-photon Cherenkov imaging counters: namely good spatial and time resolutions, large gains (single photo-electron sensitivity), relatively low mass and easy construction - thanks to the intrinsic robustness of the PCB electrodes. To advance future developments of GPMs, one of the key ingredients is the possibility to produce, with good quality and yield, THGEM-like foils of large surfaces coated with CsI UV-sensitive photocathodes. There is an ongoing $R\&D$ within the RD51 collaboration to optimize THGEM geometry and to study charging up effects, gain stability and maximum achievable gain (similar to GEMs). Fig. 9c shows a first 60×60 cm^2 THGEM foil produced in cooperation with industry (ELTOS, Italy) [136].

a) b) c)

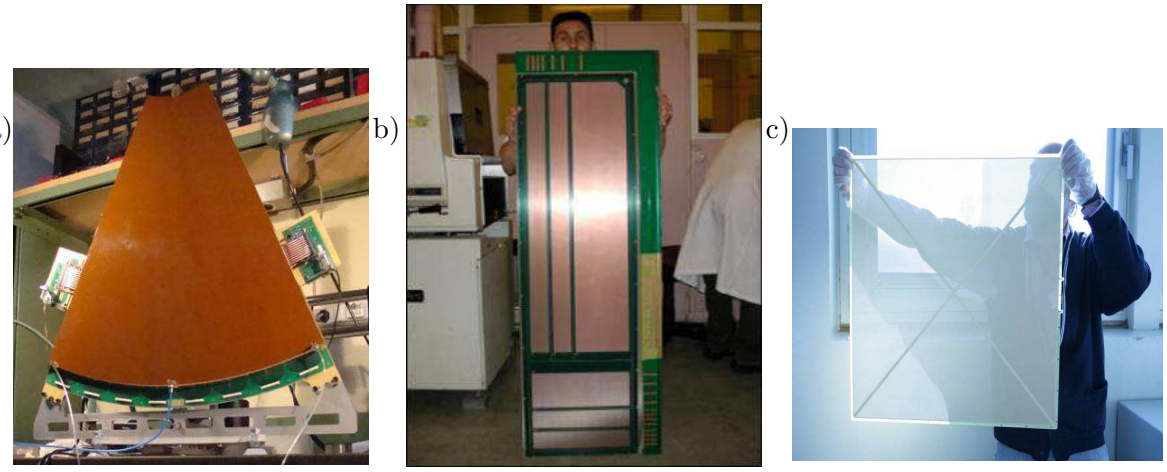


Figure 9: a) The triple-GEM prototype of 66×66 cm^2 active area, using single-mask GEM technology, for TOTEM experiment; b) Large area "Bulk" Micromegas prototype of 40×130 cm^2 size for the sLHC ATLAS muon system upgrade; c) First 60×60 cm^2 THGEM foil produced for the COMPASS RICH upgrade.

The development of large-area position-sensitive photon detectors, with visible sensitive photocathodes (e.g. bialkali), could lead to numerous spin-off, beyond the Cherenkov light imagers. Most commonly-used in the visible range are vacuum photomultipliers (PMTs), with rather limited module size and bulky geometry due to mechanical constraints on the glass vacuum envelope. A possible alternative is to use gas-filled photomultipliers at atmospheric pressure; a proof of principle of visible-sensitive GPM was demonstrated with MPGDs [103,137]. Future studies with large-area detection and visible-sensitive PC are being planned within the RD51 collaboration.

7 Pixel readout for micro-pattern gas detectors

Coupling of the micro-electronics industry together with advanced PCB technology has been very important for the development of modern gas detectors with increasingly smaller pitch size. The fine granularity and high-rate capability of micro-pattern devices can be further exploited by introducing high-density pixel readout with a size corresponding to the intrinsic width of the detected avalanche charge. However, for a pixel pitch of the order of 100 μm, technological constraints severely limit the maximum number of channels that can be brought to the external front-end electronics. While the standard approach to readout MPGDs is a

segmented strip or pad plane with front-end electronics attached through connectors from the backside, an attractive possibility is to use CMOS pixel chip, assembled directly below the GEM or Micromegas amplification structures, and serving as integrated device hosting the input pad, the preamplification and the digitization of the signals [29,30,31,32]. Due to the strong electric field in the GEM or Micromegas amplification structures, primary electron initiates avalanche, and the resulting charge signal activates the preamp-shaper-discriminator circuitry, integrated in the underlying active layers of the CMOS technology. Using this approach, gas detectors can reach the level of integration, compactness and resolving power typical of solid-state pixel devices.

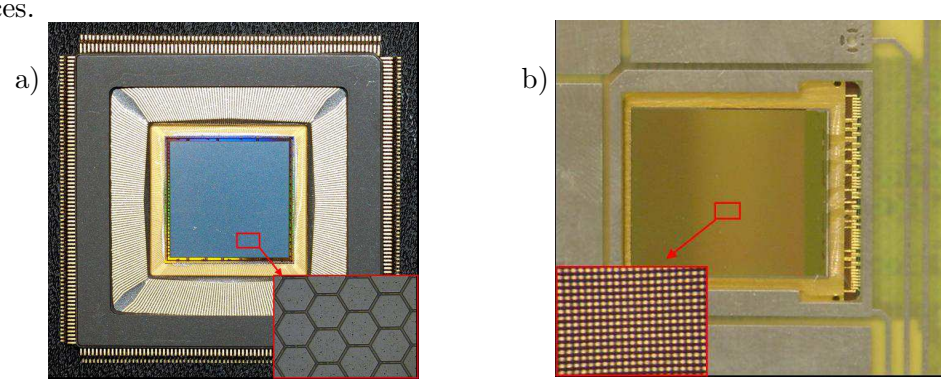


Figure 10: a) Photo of the analog CMOS ASIC with hexagonal pixels, bonded to the ceramic package; b) Photo of the Medipix2 chip; a 25 μm wide conductive bump bond openings, used for electron collection, are seen as a matrix of dots.

The combination of GEM detector and an analog, low-noise and high granularity (50 μm pitch) CMOS pixel ASIC, comprising pixellated charge collecting anode and readout electronics, can bring large improvement in sensitivity, at least 2 orders of magnitude, compared to traditional X-ray polarimeters (based on Bragg diffraction or Compton scattering) [139,140,141]. Moreover, scattering polarimeters are practically insensitive below 5 keV and are background limited, while Bragg crystal polarimeters are efficient only around a narrow band fulfilling the Bragg condition. In contrary, the pixel readout of MPGDs allows to reconstruct individual low-energy (2-3 keV) photo-electron tracks with a length as short as few hundred microns; the total charge collected in the pixels is proportional to the X-ray energy. The high detector granularity allows to recognize the initial part of the track, before it is distorted by Coulomb scattering, through the localization of absorption point of the photon and then to estimate the photo-electron emission direction. Finally, the degree of X-ray polarization is computed from the distribution of reconstructed track angles, since the photo-electron is emitted mainly in the direction of photon electric field. Three ASIC generations of increased complexity and size, reduced pitch and improved functionality have been designed and built [30,142,143,144] (see Fig.10a). The third ASIC version, realized in 0.18 μm CMOS technology, includes self-triggering capability and has 105600 hexagonal pixels with a 50 μm pitch, corresponding to an active area of 15×15 mm^2. Single GEM detector coupled to such a CMOS pixel chip can convert photons in the energy range from a few keV up to tens of keV, by choosing the appropriate gas mixture, and is able to simultaneously produce high resolution images (50 μm), moderate spectroscopy (15% FWHM at 6 keV) and fast timing (30 ns) signals. At the focal plane of the large area mirror like XEUS telescope, the novel device will allow to perform energy-resolved polarimetry at the level of few % on many galactic and extragalactic sources with photon fluxes down to one milliCrab in one day [143,144].

The original motivation of combining a MPGD with Medipix2 [145] and Timepix [146] chips was the development of a new readout system for a large TPC at the future Linear Collider. The digital Medipix2 chip was originally designed for single photon counting by means of a semiconductor X-ray sensor coupled to the chip. In gas detector applications, the chip is placed

in the gas volume without any semiconductor sensor, with GEM or Micromegas amplification structure above it [31,147,32]. Approximately 75 % of every pixel in the Medipix2 matrix is covered with an insulating passivation layer. Hence, the avalanche electrons are collected on the metalized input pads, exposed to the gas (see Fig. 10b). The Timepix chip, which is a modification of the Medipix2 chip, yields timing and charge measurements as well as precise spatial information in 3D of individual electron clusters. The Timepix ASIC sensitive area is arranged as a square matrix of 256 x 256 pixels of 55 x 55 μm^2 size, resulting in a total detection area of $\sim 14 \times 14$ mm^2, which represents 87 % of the entire surface area. The chip is designed and manufactured in a six-metal 0.25 μm CMOS technology and contains ∼50 million transistors. Each pixel in the chip matrix can be programmed to record either the arrival time of the avalanche charge signal with respect to an external shutter ("TIME" mode) or the 14-bit counter is incremented as long as the signal remains above the threshold (Time Over Threshold "TOT" mode), thus providing pulse-height information. The operation of MPGD with Timepix chip has demonstrated the possibility to reconstruct 3D-space points of individual primary electron clusters with $\sim 30 - 50$ μm spatial resolution and event-time resolution with ns precision (see Fig. 11b) [148,149,150]. Thanks to these developments, a micro-pattern device with CMOS readout can serve as a high-precision "electronic bubble chambers" (see Fig. 11a).

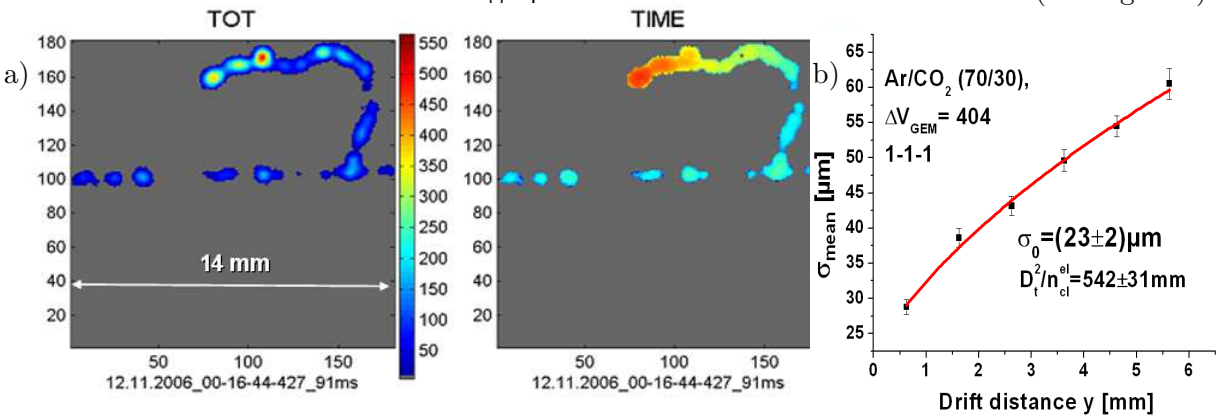


Figure 11: a) Image of the 5 GeV electron track recorded at the DESY testbeam with triple-GEM detector and TimePix CMOS ASIC operated in the mixed mode: every second pixel is operated in the "TOT"/"TIME" modes in the "chess board" fashion. The x, y-axis represent chip sensitive area, obtained by mapping the original data (matrix of 256 × 256 pixels of 55 μm pitch) into a 181 × 181 pixels matrix with a pitch of 78 μm. The color is the measure of the time-over-threshold and drift time information, respectively; b) Spatial resolution as a function of drift distance in Ar/CO_2(70:30) mixture and triple-GEM/Medipix2 detector.

An elegant solution for the construction of the Micromegas with pixel readout is the integration of the amplification grid and CMOS chip by means of an advanced "wafer post-processing" technology [33]. With this technology, the structure of thin (1 μm) aluminum grid is fabricated on top of an array of insulating (SU-8) pillars of typically 50 μm height, which stand above the CMOS chip, forming an integrated readout of the gaseous detector (see Fig. 12a). This technology is called "InGrid" (developed by the collaboration of MESA+ institute of the University of Twente and NIKHEF) and allows an accurate alignment of hexagonal grid holes ($\sim$ 60 μm pitch) with pixel input pads, sub-micron precision in the grid hole diameter and a constant thickness of the avalanche gap, which results in a uniform gas gain. The process uses standard photo-lithography and wet etching techniques and is CMOS compatible. It can be used to equip both single chips and chip wafers with Micromegas grid. Amongst the most critical items that may affect the long-term operation of "InGrid" concept is the appearance of breakdown across the 50-100 μm amplification gap. This is a critical issue for Micromegas with CMOS readout, where a multiplication grid is placed directly above the naked Timepix chip, since for single stage amplification discharges in presence of heavy ionizing particles can not be completely eliminated.

One way to achieve protection is to cover the CMOS chip with a thin layer (3 to 20 μm)

of highly resistive amorphous silicon or silicon nitride (Si_3N_4) deposited directly on top of the Timepix ASIC [151,152]. This protective cover, called "SiProt", intends to protect the chip from high instantaneous spark currents, which could destroy the chip, and from the the evaporation of the Timepix metal input pads during sparks (see Fig. 12b). The performance of the "InGrid" detector with 4 μm "SiProt" layer is illustrated in Fig. 12c for 2 GeV electron beam at DESY. Due to its high sensitivity, "InGrid" detector can resolve single primary electrons [31,153]. The color is a measure of the electron arrival time in "TOT" mode, red color corresponds to the primary ionization electrons produced close to the chip surface. The spread of the clusters in Fig. 12c indicates that the diffusion increases with the distance from the chip. The time range in He/iC_4H_{10} mixture is larger than in Ar/iC_4H_{10}, which indicates lower drift velocity in He-based mixture, while the primary ionization density (number of active pixels) is higher in Ar-based mixture [154]. The "InGrid" device with a narrow (1-1.5 mm) drift gap ("GOSSIP") is currently proposed as one of the possible upgrade options for the ATLAS tracking system at sLHC, aiming for a spatial precision of about 20 μm [94].

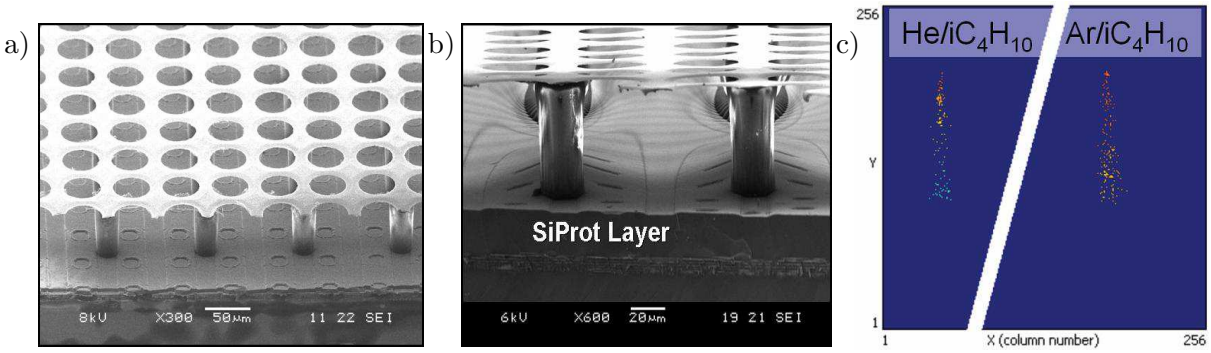


Figure 12: a) The Scanning Electron Microscopy (SEM) image of the "InGrid" detector: a Timepix chip, resistive silicon-nitride (Si_3N_4) protection layer and insulating SU-8 pillars supporting a perforated Al grid. The pillars are placed at the intersections of four adjacent pixels; the circular holes in the grid are centered onto the input pad of each pixel; b) Photo of the "InGrid" structure with 7 μm Si_3N_4 protection layer; c) Images of 2 GeV electron tracks recorded with "InGrid" detector in Ar/C_4H_{10} and He/C_4H_{10} mixtures in "TIME" mode; the color is a measure of the arrival time of electrons.

One of the most exciting future applications of GEM and Micromegas devices with CMOS multi-pixel readout could be position sensitive single photon detection. Recently, a UV photodetector based on a semitransparent CsI photocathode followed by the fine-pitch GEM foil, that matches the pitch of a pixel ASIC (50 μm), has shown excellent imaging capabilities [155]. The photoelectron emitted from CsI layer drifts into a single GEM hole and initiates an avalanche, which is then collected on the pixel CMOS analog chip. Due to the high granularity and large S/N of the read-out system, the "center of gravity" of the single electron avalanche corresponds to the center of GEM hole. Accumulating thousands of such events produces "self-portrait" of the GEM amplification structure, shown in Fig. 13 (a) and allows to achieve superior single electron avalanche reconstruction accuracy of 4 μm rms [155]. Another monolithic gaseous UV-photon imaging device is based on the "InGrid" concept and reflective CsI photocathode deposited on Micromegas grid. The photocathode deposition and its operation is found to be adequate in combination with both the "InGrid" detector and Timepix chip. Fig. 13b shows image recorded with a steel mask placed in front of the "InGrid" detector under UV-photon irradiation. The detector operated reliably in He/iC_4H_{10} mixture with single electron extraction efficiency of ~ 50 % and a maximum achievable gain of $\sim 6 \times 10^4$. These results encourage further developments towards high-resolution UV photon devices, based on combination of MPGD with CMOS pixel readout. Futhermore, being made of UHV-compatible materials, "InGrid" concept could be used in cascaded visible light-sensitive imaging gas photomultipliers.

A key point that has to be solved to allow CMOS pixel readout of MPGD for applica-

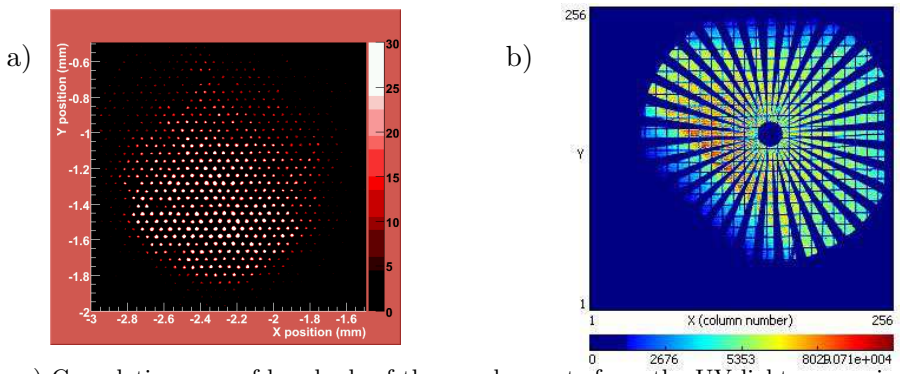


Figure 13: a) Cumulative map of hundreds of thousands events from the UV light conversion in the semitransparent CsI photocathode of the detector producing a kind of "self-portrait" of the GEM amplification structure. The white spots correspond to the individual GEM holes at 50 μm pitch; b) 2D image of the steel mask under irradiation of the "InGrid" detector with reflective CsI photocathode in He/iC_4H_{10} (80:20) mixture.

tions in various fields of fundamental science and beyond is the production of large area detectors. Presently prototypes under construction rely at maximum on 2×4 chips integrated readout [97,157]. Going to large surface detector requires solution for the dead space on one side of the Timepix chip, where the electrical connections enter the chip (see Fig. 10b). A first solution relies on etching of "through-silicon vias" on the Timepix chip that allows to bring out the signals and services on the backside of the chip using "through-wafer-vias" technology [158,159]. This is known as "via-last" operation: the existing Timepix wafers are modified by etching "in-vias" connections after the CMOS wafer production step is completed. In order to move from 3-side tileable detectors to 4-side, all common circuitry (bias, converters, ...) needs to be spread over the chip area which is nowadays become possible thanks to the progress in 3D micro-electronics, where the different functions can be realized on different tiers and connected thanks to "through-silicon vias" and inter-connects. However, a major R&D effort is required in the future to fully exploit this potential.

Properly integrated into large systems (including development of large area MPGD based on the integrated multi-chip CMOS ASICs), the pixel readout may open new opportunities for an advanced Compton Telescope [160,161], detection of Axions and Weakly Interacting Massive Particles [162], neutrino-less double beta decay experiments [163] and 3D imaging of nuclear recoils. The primary advantage of a gaseous tracker with pixel readout is that the direction of the Compton electron or the low energy nuclear recoil can be reconstructed far more accurately than in any other detection medium.

8 Summary

Radiation detection and imaging with gas-avalanche detectors, capable of economically covering large detection volumes with a low material budget, have been playing an important role in many fields. While extensively employed at the LHC, RHIC, and other advanced HEP experiments, present gaseous detectors (wire-chambers, drift-tubes, resistive-plate chambers and others) have limitations which may prevent their use in future experiments.

The possibility of producing micro-structured semi-conductor devices (with structure sizes of tens of microns) and corresponding highly integrated readout electronics led to the success of semi-conductor (in particular silicon) detectors to achieve unprecedented space-point resolution. Micro-pattern gas-amplification structures now open the possibility to apply the same technology to gaseous detectors and enable a plethora of new detector concepts in science and industry, in medical and commercial applications. Microelectronics needs to keep up with the state-of-the-art developed by the microelectronics industry and the interconnection between electronics and detectors needs to be improved to reduce the complexity and the material of interconnect

technologies.

The RD51 collaboration at CERN, approved in December 2008, aims at facilitating the development of advanced gas-avalanche detector technologies and associated electronic-readout systems, for applications in basic and applied research. The main objective of the R&D program is to advance technological development and application of micro-pattern gaseous detectors. The RD51 collaboration involves $\sim$ 430 authors, 73 Universities and Research Laboratories from 25 countries in Europe, America, Asia and Africa. All partners are already actively pursuing either basic- or application-oriented R&D involving a variety of MPGD concepts. The collaboration established common goals, like experimental and simulation tools, characterization concepts and methods, common infrastructures at test beams and irradiation facilities, and infrastructure for MPGD production. More information can be found at the RD51 collaboration webpage [34].

References

1. H. Geiger, E. Rutherford, *Proc. Royal Soc. A* **81**, 141 (1908).
2. H. Geiger, W. Mueller, *Phys. Zeits.* **29**, 839 (1928).
3. G. Charpak *et al*, *Nucl. Instrum. Methods* A **62**, 262 (1968).
4. F. Sauli, "Principles of Operation of Multiwire Proportional and Drift Chambers", *CERN* **77-09** (1977).
5. G. Charpak, F. Sauli, *Ann. Rev. Nucl. Part. Sci.* **34**, 285 (1984).
6. F. Sauli, "From Bubble Chambers to Electronic Systems: 25 Years of Evolution in Particle Detectors at CERN", *CERN PH-EP* **2004-040** (2004).
7. C. Grupen, *Particle Detectors* (Cambridge Univ. Press, 1996).
8. W. Blum, W. Riegler, L. Rolandi, *Particle Detection with Drift Chambers* (Springer-Verlag, 2008).
9. A. H. Walenta *et al*, *Nucl. Instrum. Methods* A **92**, 373 (1971).
10. R. Bouclier *et al*, *Nucl. Instrum. Methods* A **265**, 78 (1988).
11. H. Drumm *et al*, *Nucl. Instrum. Methods* A **176**, 333 (1980).
12. D.R. Nygren, J.N. Marx, *Phys. Today,* **31, Vol. 10** (1978).
13. A. H. Walenta, IEEE Trans. Nucl. Sci. (TNS), **Vol. 26**, 73 (1979).
14. G. Charpak, F. Sauli, *Phys. Lett.* B **78**, 523 (1978).
15. J. Seguinot, T. Ypsilantis, *Nucl. Instrum. Methods* A **142**, 377 (1977).
16. A. Oed, *Nucl. Instrum. Methods* A **263**, 351 (1988).
17. A. Barr *et al*, *Nucl. Phys.* B (Proc. Suppl.) **61B**, 264 (1998).
18. A. Oed, *Nucl. Instrum. Methods* A **490**, 223 (2002).
19. F. Sauli, *Nucl. Instrum. Methods* A **386**, 531 (1997).
20. Y. Giomataris *et al*, *Nucl. Instrum. Methods* A **376**, 29 (1996).
21. F. Sauli, A. Sharma, *Ann. Rev. Nucl. Part. Sci.* **49**, 341 (1999).
22. M. Titov, *Nucl. Instrum. Methods* A **581**, 25 (2007).
23. M. Titov *et al*, IEEE Trans. Nucl. Sci. (TNS), **Vol. 49(4)**, 1609 (2002).
24. M. Titov, "Radiation Damage and Long-Term Aging in Gas Detectors,", *arXiv: physics/***0403055**; *Proc. of the Workshop of the INFN ELOISATRON Project*, "Innovative Detectors For Super-Colliders," Erice, Italy, Sept.28 - Oct.4 (2003).
25. L. Periale *et al*, *Nucl. Instrum. Methods* A **478**, 377 (2002).
26. R. Chechik *et al*, *Nucl. Instrum. Methods* A **535**, 303 (2004).
27. A. Breskin *et al*, *Nucl. Instrum. Methods* A **598**, 107 (2009).
28. A. Di Mauro *et al*, *Nucl. Instrum. Methods* A **581**, 225 (2007).
29. E. Costa *et al*, *Nature* **411**, 662 (2001).
30. R. Bellazzini *et al*, *Nucl. Instrum. Methods* A **535**, 477 (2004).
31. M. Campbell *et al*, *Nucl. Instrum. Methods* A **540**, 295 (2005).

32. A. Bamberger *et al*, *Nucl. Instrum. Methods* A **573**, 361 (2007).
33. M. Chefdeville *et al*, *Nucl. Instrum. Methods* A **556**, 490 (2006).
34. `http://rd51-public.web.cern.ch/RD51-Public`
35. "Review of Particle Physics" (By Particle Data Group), `Chapters 28.7.1-28.7.3 ''Gaseous Detectors''` written by F. Sauli, M. Titov, *Phys. Lett.* B **667**, 292 (2008).
36. `http://rjd.web.cern.ch/rjd/cgi-bin/cross`
37. A. Peisert, F. Sauli, "Drift and Diffusion of Electrons in Gases", *CERN* **84-08** (1984).
38. S. Biagi, *Nucl. Instrum. Methods* A **421**, 234 (1999).
39. `http://consult.cern.ch/writeup/magboltz/`
40. L.G. Christophorou *et al*, "Electron Interaction in CF_4", *J. Phys. Chem. Ref. Data* **Vol.25, No.5**, 1341 (1996).
41. E. McDaniel, E. Mason, *The Mobility and Diffusion of Ions in Gases* (Wiley, 1973).
42. G. Shultz *et al*, Rev. Phys. Appl. **12**, 67 (1977).
43. G. Charpak *et al*, *Nucl. Instrum. Methods* A **167**, 455 (1979).
44. A. Breskin *et al*, *Nucl. Instrum. Methods* A **124**, 189 (1975).
45. A. Breskin *et al*, *Nucl. Instrum. Methods* A **156**, 147 (1978).
46. D. Nygren *et al*, *PEP-PROPOSAL-004, Appendix A 6,* (1976).
47. D. Decamp *et al*, *Nucl. Instrum. Methods* A **294**, 121 (1990).
48. Y. Sacquin *et al*, *Nucl. Instrum. Methods* A **323**, 209 (1992).
49. S. Afanasev *et al*, *Nucl. Instrum. Methods* A **430**, 210 (1999).
50. H. Wieman *et al*, IEEE Trans. Nucl. Sci. (TNS), **Vol. 44(3)**, 671 (1997).
51. `http://www.ansoft.com`
52. D. Antonczyk *et al*, *Nucl. Instrum. Methods* A **565**, 551 (2006).
53. T. Meyer, "System Aspects of (Gaseous) Tracking Detectors", *Proc. of the Workshop of the INFN ELOISATRON Project*, "Innovative Detectors For Super-Colliders," Erice, Italy, Sept.28 - Oct.4 (2003).
54. M. Aleksa *et al*, *Nucl. Instrum. Methods* A **446**, 435 (2000).
55. R. Bouclier *et al*, *Nucl. Instrum. Methods* A **381**, 289 (1996).
56. V.Peskov *et al*, *Nucl. Instrum. Methods* A **397**, 243 (1997).
57. Yu. Ivaniouchenkov *et al*, *Nucl. Instrum. Methods* A **422**, 300 (1999).
58. A. Bressan *et al*, *Nucl. Instrum. Methods* A **424**, 321 (1999).
59. Yu. Ivaniouchenkov *et al*, IEEE Trans. Nucl. Sci. (TNS), **Vol. 45(3)**, 258 (1998).
60. P.Fonte *et al*, IEEE Trans. Nucl. Sci. (TNS), **Vol. 46(3)**, 321 (1999).
61. C. Iacobaeus *et al*, IEEE Trans. Nucl. Sci. (TNS), **Vol. 49(4)**, 1622 (2002).
62. V. Peskov, P. Fonte, "Research on discharges in micropattern and small gap detectors", *arXiv:* **0911.0463**(2009).
63. A. Bondar *et al*, *Nucl. Instrum. Methods* A **556**, 495 (2006).
64. A. Bressan *et al*, *Nucl. Instrum. Methods* A **425**, 262 (1999).
65. S. Bachmann *et al*, *Nucl. Instrum. Methods* A **438**, 376 (1999).
66. S. Bachmann *et al*, *Nucl. Instrum. Methods* A **470**, 548 (2001).
67. S. Bachmann *et al*, *Nucl. Instrum. Methods* A **479**, 294 (2002).
68. A. Breskin *et al*, *Nucl. Instrum. Methods* A **513**, 250 (2003).
69. J.F.C.A. Veloso *et al*, *Rev. Sci. Instr.* **71(6)**, 2371 (2000).
70. A. Lyashenko *et al*, *JINST* **2, P08004** (2007).
71. Y. Giomataris, *Nucl. Instrum. Methods* A **419**, 239 (1998).
72. J. Derre *et al*, *Nucl. Instrum. Methods* A **459**, 523 (2001).
73. G. Charpak *et al*, *Nucl. Instrum. Methods* A **478**, 26 (2002).
74. J. Derre *et al*, *Nucl. Instrum. Methods* A **449**, 314 (2000).
75. Y. Giomataris *et al*, *Nucl. Instrum. Methods* A **560**, 405 (2006).
76. S. Anvar *et al*, *Nucl. Instrum. Methods* A **602**, 415 (2009).

77. S. Andriamonje *et al*, *JINST* **5, P02001** (2010).
78. L. Periale *et al*, IEEE Trans. Nucl. Sci. (TNS), **Vol. 50(4)**, 809 (2003).
79. C. Shalem *et al*, *Nucl. Instrum. Methods* A **558**, 475 (2006).
80. R. Chechik *et al*, *Nucl. Instrum. Methods* A **553**, 35 (2005).
81. C. Azevedo *et al*, *JINST* **5, P01002** (2010).
82. R. Oliveira *et al*, *Nucl. Instrum. Methods* A **576**, 362 (2007).
83. A. Di Mauro *et al*, *Nucl. Instrum. Methods* A **581**, 225 (2007).
84. A. Di Mauro *et al*, *Nucl. Instrum. Methods* A **610**, 169 (2009).
85. B. Ketzer *et al*, *Nucl. Instrum. Methods* A **535**, 314 (2004).
86. C. Bernet *et al*, *Nucl. Instrum. Methods* A **536**, 61 (2005).
87. D. Neyret *et al*, *JINST* **4, P12004** (2009).
88. M. Alfonsi *et al*, IEEE Trans. Nucl. Sci. (TNS), **Vol. 51(5)**, 2135 (2004).
89. S. Lami, "First Test Results for the TOTEM T2 Telescope", 2009 IEEE NSS Conference Record.
90. M. Vandenbroucke, "A GEM-based TPC Prototype for PANDA", 2009 IEEE NSS Conference Record.
91. `http://hallaweb.jlab.org/12GeV/SuperBigBite/`
92. F. Simon *et al*, "The Forward GEM Tracker of STAR at RHIC", 2009 IEEE NSS Conference Record.
93. G. Barouch *et al*, *Nucl. Instrum. Methods* A **423**, 32 (1999).
94. H. van der Graaf *et al*, "Performance and prospects of GridPix and Gossip detectors", *RD51 Note, RD51-2009-006,* (2009).
95. A. Balla *et al*, "Status of the Cylindrical GEM Project for the KLOE-2 Inner Tracker", 2009 IEEE NSS Conference Record.
96. A. Aune *et al*, *Nucl. Instrum. Methods* A **604**, 53 (2009).
97. G. De Lentdecker, "A Large TPC Prototype for an ILC Detector", 2009 IEEE NSS Conference Record.
98. D.C. Arogancia *et al*, *Nucl. Instrum. Methods* A **602**, 403 (2009).
99. T. Matsuda, *JINST* **5, P01010** (2010).
100. Jaehoon Yu, "Development of GEM Based Digital Hadron Calorimeter", 2009 IEEE NSS Conference Record.
101. C. Adloff *et al*, *JINST* **4, P11023** (2009).
102. R. Chechik *et al*, *Nucl. Instrum. Methods* A **502**, 195 (2003).
103. R. Chechik, A. Breskin, *Nucl. Instrum. Methods* A **595**, 116 (2008).
104. A. Buzulutskov, *Phys. Part. Nucl.* **39**, 424 (2008).
105. Y. Giomataris, G. Charpak, *Nucl. Instrum. Methods* A **310**, 585 (1991).
106. Z. Fraenkel *et al*, *Nucl. Instrum. Methods* A **546**, 466 (2005).
107. C. Woody *et al*, "Initial Performance of the PHENIX Hadron Blind Detector at RHIC", 2009 IEEE NSS Conference Record.
108. A. Di Mauro *et al*, IEEE Trans. Nucl. Sci. (TNS), **Vol. 56(3)**, 1550 (2009).
109. L. Periale *et al*, IEEE Trans. Nucl. Sci. (TNS), **Vol. 52(4)**, 927 (2005).
110. L. Periale *et al*, *Nucl. Instrum. Methods* A **573**, 302 (2007).
111. A. Bondar *et al*, *Nucl. Instrum. Methods* A **581**, 241 (2007).
112. A. Bondar *et al*, *Nucl. Instrum. Methods* A **598**, 121 (2009).
113. C. Hagmann *et al*, IEEE Trans. Nucl. Sci. (TNS), **Vol. 51(5)**, 2151 (2004).
114. A. Rubbia, " Experiments for CP violation: A Giant liquid argon scintillation, Cerenkov and charge imaging experiment?" *arXiv: hep-ph/0402110* (2004).
115. A. Rubbia, " ArDM: A Ton-scale liquid Argon experiment for direct detection of dark matter in the universe," *arXiv: hep-ph/0510320* (2005).
116. A. Buzulutskov, *Instr. Exp. Tech.* **50**, 287 (2007).

117. C. Grignon *et al*, *Nucl. Instrum. Methods* A **571**, 142 (2007).
118. S. Duval *et al*, *JINST* **4, P12008** (2009).
119. G. Smith, "Gas-based detectors for synchrotron radiation", *Journal of Synchrotron Radiation* **13(2)**, 172 (2006).
120. D. Pacella *et al*, *JINST* **1, P09001** (2006).
121. S. Duarte Pinto *et al*, "Spherical GEMs for parallax-free detectors", 2009 IEEE NSS Conference Record.
122. S. Aune *et al*, *Nucl. Instrum. Methods* A **604**, 15 (2009).
123. J. Pancin *et al*, *Nucl. Instrum. Methods* A **524**, 102 (2004).
124. M. Houry *et al*, *Nucl. Instrum. Methods* A **557**, 648 (2006).
125. S. Andriamonje *et al*, 2004 IEEE NSS/MIC Conference Record.
126. S. Andriamonje *et al*, *Nucl. Instrum. Methods* A **562**, 755 (2006).
127. C. Iacobaeus *et al*, IEEE Trans. Nucl. Sci. (TNS), **Vol. 48**, 1496 (2001).
128. J. Ostling *et al*, IEEE Trans. Nucl. Sci. (TNS), **Vol. 50**, 809 (2003).
129. S. Fetal *et al*, *Nucl. Instrum. Methods* A **513**, 42 (2003).
130. M. Hohlmann *et al*, "Design and Construction of a First Prototype Muon Tomography System with GEM Detectors for the Detection of Nuclear Contraband," *arXiv: 0911.3203* (2009).
131. G. Charpak *et al*, " Performance of wire-type Rn detectors operated with gas gain in ambient air in view of its possible application to early earthquake predictions," *arXiv: 1002.4732* (2010).
132. G. Charpak *et al*, *JINST* **4, P12007** (2009).
133. G. Charpak *et al*, IEEE Trans. Nucl. Sci. (TNS), **Vol. 55**, 1657 (2003).
134. S. Duarte Pinto *et al*, *JINST* **4, P12009** (2009).
135. T. Alexopoulos *et al*, *JINST* **4, P12015** (2009).
136. F. Tessarotto, *Talk at the 3rd RD51 Collaboration Meeting, June 12-17 (2009), Crete, Greece.*
137. A. Lyashenko *et al*, *JINST* **4, P07005** (2009).
138. G. Charpak *et al*, *JINST* **4, P12007** (2009).
139. R. Bellazzini *et al*, "A Micro Pattern Gas Detector for X-ray polarimetry", *Proc. SPIE, Polarimetry in Astronomy,* **4843**, 372 (2003).
140. R. Bellazzini *et al*, "The sensitivity of a photoelectric X-ray polarimetry for astronomy: the impact of gas mixtures and pressure", *Proc. SPIE, Polarimetry in Astronomy,* **4843**, 394 (2003).
141. F. Muleri *et al*, *Nucl. Instrum. Methods* A **584**, 149 (2008).
142. R. Bellazzini *et al*, *Nucl. Instrum. Methods* A **560**, 425 (2006).
143. R. Bellazzini *et al*, *Nucl. Instrum. Methods* A **566**, 552 (2006).
144. R. Bellazzini *et al*, *Nucl. Instrum. Methods* A **572**, 160 (2006).
145. X. Llopart, M. Campbell, IEEE Trans. Nucl. Sci. (TNS), **Vol. 49(5)**, 2279 (2002).
146. X. Llopart *et al*, *Nucl. Instrum. Methods* A **581**, 485 (2007).
147. P. Colas *et al*, *Nucl. Instrum. Methods* A **535**, 506 (2004).
148. A. Bamberger *et al*, *Nucl. Instrum. Methods* A **581**, 274 (2007).
149. A. Bamberger *et al*, *arXiv: 0709.2837,* (2007).
150. C. Brezina *et al*, *JINST 4, P11015* (2009).
151. A. A. Aarts *et al*, "Discharge Protection and Ageing of Micromegas Pixel Detectors", 2006 IEEE NSS Conference Record.
152. M. Bosma *et al*, "Results from MPGDs with a Protected Timepix or Medipix2 pixel sensor as active anode", 2007 IEEE NSS Conference Record.
153. V. M. Blanco Carballo *et al*, *Nucl. Instrum. Methods* A **583**, 42 (2007).
154. Y. Bilevych *et al*, "The Performance of GridPix Detectors", 2009 IEEE NSS Conference

Record.
155. R. Bellazzini *et al*, *Nucl. Instrum. Methods* A **581**, 246 (2007).
156. J. Melai *et al*, *arXiv: 1003.2083,* (2010).
157. J. Kaminski, Talk at the 4th RD51 Collaboration Meeting, Nov. 23-25 (2009).
158. K. Takahashi *et al*, *Microelectronics Realibility*4312672003.
159. E. Heijne, *Nucl. Instrum. Methods* A **541**, 274 (2005).
160. A. Takada *et al*, *Nucl. Instrum. Methods* A **546**, 258 (2005).
161. K. Miuchi *et al*, *Nucl. Instrum. Methods* A **576**, 43 (2007).
162. S. Ahlen *et al*, *Intl. Jour. Mod. Phys. A,* **25(1)**, 1 (2010).
163. V. Blanco Carballo *et al*, *JINST 5, P02002* (2010).